



# CCR5-ligand decorated rilpivirine lipid-based nanoparticles for sustained antiretroviral responses

Received: 16 May 2024

Accepted: 17 December 2024

Published online: 08 January 2025

 Check for updates

Milankumar Patel<sup>1,6</sup>, Sudipta Panja<sup>1,6</sup> , Lubaba A. Zaman<sup>1</sup>, Pravin Yeapuri<sup>1</sup>, Shaurav Bhattarai<sup>1</sup>, Santhi Gorantla<sup>1</sup>, Linda Chang<sup>2,3</sup>, Alonso Heredia<sup>4</sup>, Piotr Walczak<sup>2</sup>, Brandon Hanson<sup>1</sup>, Samuel M. Cohen<sup>5</sup>, Bhavesh D. Kevadiya<sup>1</sup> & Howard E. Gendelman<sup>1</sup> 

Antiretroviral therapy (ART) improves the quality of life for those living with the human immunodeficiency virus type one (HIV-1). However, poor compliance reduces ART effectiveness and leads to immune compromise, viral mutations, and disease co-morbidities. Here we develop a drug formulation in which a lipid-based nanoparticle (LBNP) carrying rilpivirine (RPV) is decorated with the C-C chemokine receptor type 5 (CCR5) targeting peptide. This facilitates extended drug persistence within myeloid cells. Particle delivery to viral reservoirs is tracked by positron emission tomography. The CCR5-mediated LBNP cell uptake and retention reduce HIV-1 replication in human monocyte-derived macrophages and infected humanized mice (hu mice). Focused ultrasound with microbubbles mediated blood brain barrier (BBB) disruption allows the CCR5-targeted LBNP to penetrate the BBB and reach brain myeloid cells. These findings offer a role for CCR5-targeted therapeutics in antiretroviral delivery to optimize HIV suppression.

The human immunodeficiency virus (HIV) global epidemic began in 1981 and has led to 40 million deaths and equal numbers of infected people<sup>1,2</sup>. The HIV-1 replication suppressed by antiretroviral therapy (ART) has markedly improved disease outcomes. However, the viral DNA integration into the host genome defines microbial latency, demonstrating that HIV-1 can circumvent antiretroviral immunity with continuous HIV comorbidities<sup>3,4</sup>. ART faces challenges due to its failure to eliminate infection, the need for strict regimen adherence, and drug-related toxicities. ART bioavailability to the lymphoid, gut, central nervous system (CNS), heart, liver, and kidney tissues is added to this list of drug challenges<sup>5-7</sup>. Limitations in ART tissue penetration are linked to drug pharmacologic properties or ART pauses, where both lead to the emergence of viral drug resistance<sup>8</sup>.

Therefore, strict adherence to lifelong ART is required to maintain viral suppression<sup>9</sup>.

Improved drug delivery has an underexplored potential for improved therapeutic outcomes. One way this can be further improved is through functional LBNPs. However, this alone may not allow drug accumulation to viral reservoirs<sup>10</sup>. Success is made by optimizing antiretroviral drug (ARV) tissue and cell-specific targeting. LBNPs may improve ARV pharmacodynamics by increasing drug circulation time and bioavailability<sup>7,9,11</sup>. LBNP composition and decoration with targeting ligand enable ARV cell depots and enhance delivery to viral reservoirs<sup>12</sup>. Furthermore, if a targeted system is developed, it can improve ARV's residence time by creating a cell depot that could sustain antiretroviral activities.

<sup>1</sup>Department of Pharmacology and Experimental Neuroscience, University of Nebraska Medical Center, Omaha, NE 68198, USA. <sup>2</sup>Departments of Diagnostic Radiology & Nuclear Medicine and Neurology, University of Maryland School of Medicine, Baltimore, MD, USA. <sup>3</sup>Department of Neurology, Johns Hopkins University School of Medicine, Baltimore, MD, USA. <sup>4</sup>Institute of Human Virology, University of Maryland School of Medicine, Baltimore, MD, USA. <sup>5</sup>Department of Pathology, Microbiology, and Immunology, and the Buffett Cancer Center, University of Nebraska Medical Center, Omaha, NE 68198, USA. <sup>6</sup>These authors contributed equally: Milankumar Patel, Sudipta Panja.  e-mail: [sudipta.panja@unmc.edu](mailto:sudipta.panja@unmc.edu); [hlegendel@unmc.edu](mailto:hlegendel@unmc.edu)

Considering this idea, we created a CCR5-receptor targeting peptide decorated RPV LBNP. The radioactive nanoprobe,  $^{64}\text{CuInEuS}_2$  was synthesized and encased into the LBNP with RPV to monitor tissue delivery using positron emission tomography (PET). The created LBNP-RPV-CCR5 formulation led to viral suppression in viral reservoir tissues and cells in HIV-1<sub>ADA</sub>-infected hu mice<sup>13</sup>. ARV myeloid-targeted formulations produced cell depots and improved their responses.

## Results and discussion

### Synthesis and characterization of $^{64}\text{CuInEuS}_2$ nanoprobes

Theranostic LBNPs affirm the simultaneous delivery of a therapeutic drug and an imaging nanoprobe. Specifically, the antiretroviral drug RPV was chosen as the therapeutic payload, while the radioactive nanoprobe  $^{64}\text{CuInEuS}_2$  was selected for imaging purposes. The beta-emitting properties of  $^{64}\text{CuInEuS}_2$ , coupled with its favorable radioactive half-life (12.7 h), make it ideal for PET, computed tomography (CT), and magnetic resonance imaging (MRI) tri-modality imaging.

Furthermore, its biocompatibility and ability to induce biological responses were significant factors in its selection<sup>14,15</sup>. The chelator-free  $^{64}\text{CuInEuS}_2$  nanoprobe was synthesized by solvothermal methods using thioacetamide, europium (III) chloride hexahydrate, indium (III) chloride dihydrate, and copper (II) chloride dihydrate at an appropriate molar ratio. The high boiling solvent, oleylamine was selected for solvothermal synthesis to achieve a narrowly dispersed nanoprobe. The nanoprobe morphology was examined under transmission electron microscopy (TEM) which revealed a narrowly dispersed rod-shaped nanostructure with an average diameter of 15 nm and an average length of 65 nm (Fig. 1A). High-resolution TEM images demonstrated the crystal lattice of the nanoprobe (Fig. 1B). The presence of crystallinity was further confirmed by the appearance of X-ray diffraction (XRD) peaks at  $2\theta$  of 14.1°, 16.8°, 25.4°, 26.2°, 27.8°, 28.0°, 30.0°, 32.5°, 34.1°, 37.4°, 39.2°, 39.5°, 45.3°, 46.0° and 52.2°, and selected area electron diffraction patterns (Fig. 1C and Fig. S1A). High-angle annular dark-field scanning TEM showed the coexistence of

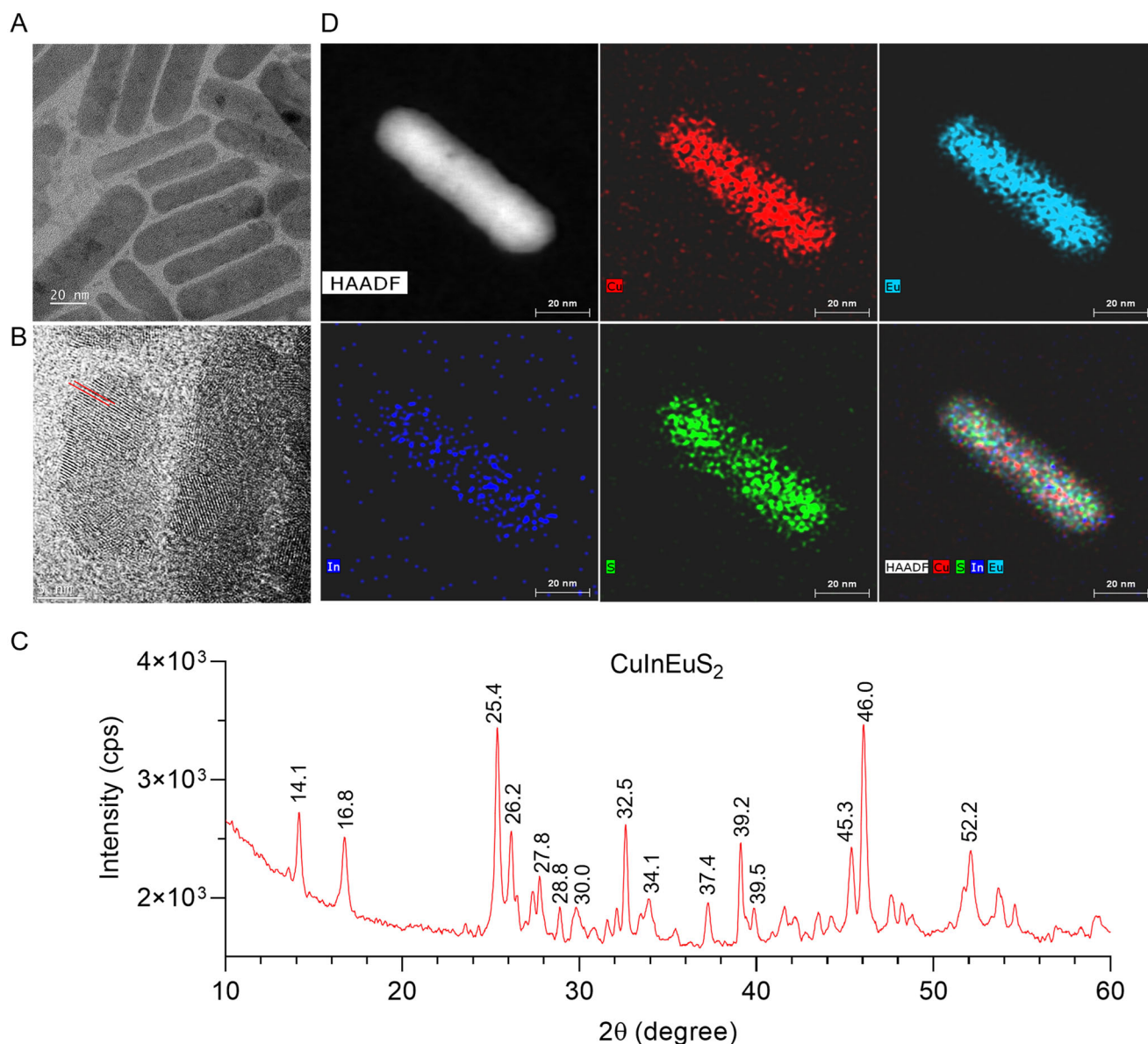


**Fig. 1 | Morphological characterization of the multimodal  $\text{CuInEuS}_2$  nanoprobe.** **A, B** Transmission electron microscope images of the multimodal rod-shaped nanoprobes.  $\text{CuInEuS}_2$  and its crystal lattice (red lines) are illustrated. **C** A scanning transmission electron microscopy (STEM) map shows elemental localization within the nanoprobe from a corresponding high-angle annular dark-field electron

microscopy image. The map shows the presence of copper (red), indium (blue), europium (cyan), and sulfur (green) in the nanoprobe. The reproducibility of  $\text{CuInEuS}_2$  synthesis was verified at least 10 independent reactions. **D** XRD pattern of  $\text{CuInEuS}_2$  nanoprobe demonstrates a crystal structure.

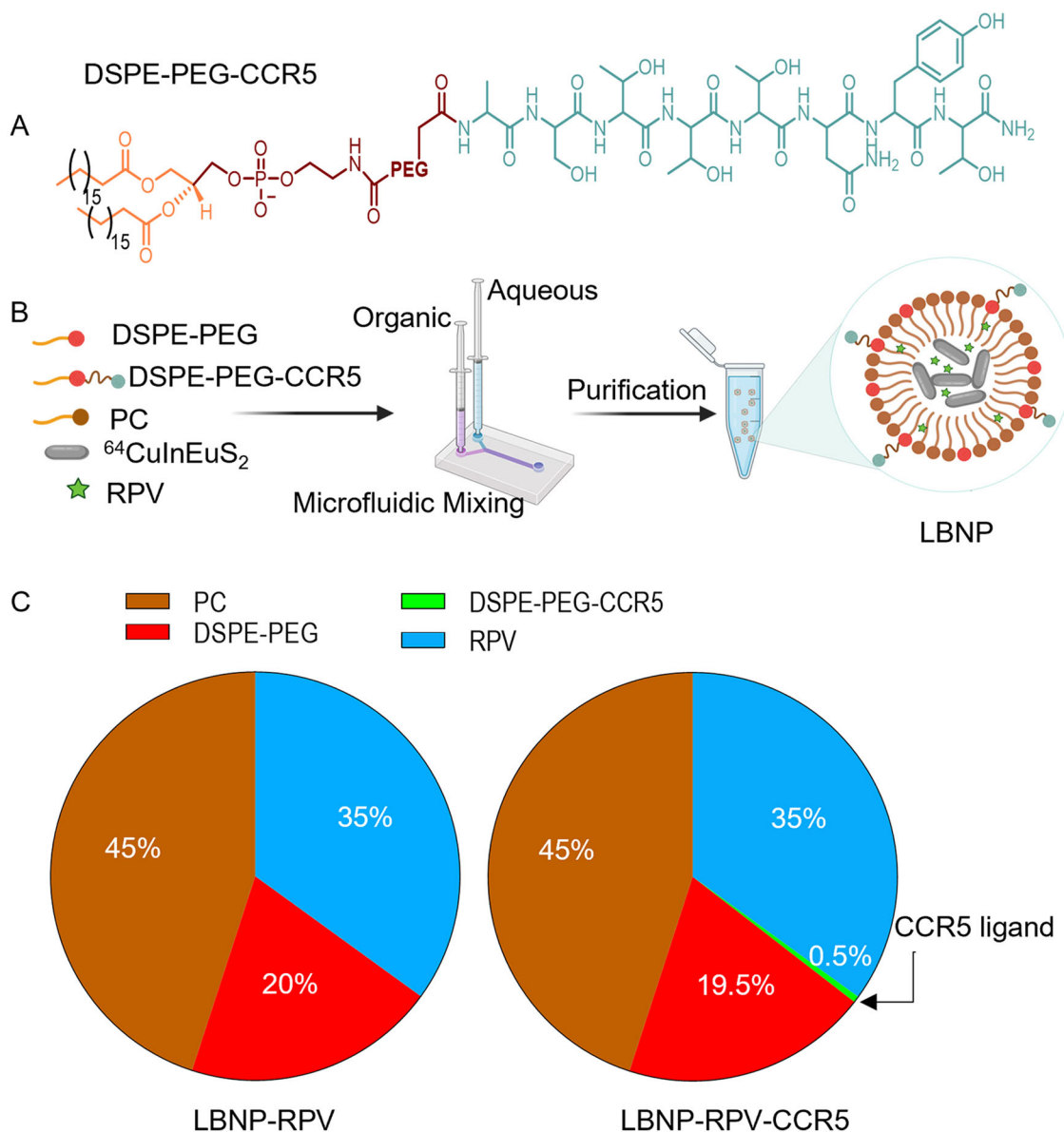


**Fig. 2 | Synthesis, formulation, and composition of LBPNs.** **A** The chemical structure of the DSPE-PEG conjugated CCR5-receptor targeting peptide is shown. **B** Schematic illustration of the formulation of LBPNs by microfluidic mixing,

created in BioRender<sup>35</sup>. **C** The molar percentages of various lipids used in LBPN formulation are presented in the pie chart.

copper (red), indium (blue), europium (cyan), and sulfur (green) in the multimodal  $^{64}\text{CuInEuS}_2$  nanoprobe (Fig. 1D). The results were further supported by the appearance of the elements trace in energy-dispersive X-ray spectroscopy (Fig. S1B).  $^{64}\text{CuInEuS}_2$  was subjected to X-ray photoelectron spectroscopy (XPS) to evaluate its surface elemental composition (Fig. S2). The appearance of binding energy peaks corresponding to Eu 3d (at 1134.26 and 1164.40 eV), Cu 2p (at 931.87 and 951.69 eV), In 3d (at 444.07 and 451.58 eV), and S 2p (at 161.09 and 168.47 eV) demonstrated their presence within the nanoprobe.

#### Synthesis of a CCR5-peptide conjugated formulation

To formulate the CCR5-receptor-targeted LBPN, a linear CCR5-peptide (D-Ala-Ser-Thr-Thr-Thr-Asn-Tyr-Thr-NH<sub>2</sub>) was chosen as the targeting ligand because this sequence has been shown to selectively bind to the CCR5 receptor<sup>16,17</sup>. The free -NH<sub>2</sub> group on the CCR5-peptide was conjugated to DSPE-PEG-NHS by an activated acid amine coupling reaction (Fig. 2A). The <sup>1</sup>H NMR spectra of the DSPE-PEG conjugated peptide showed chemical shifts at 0.8 and 1.27 ppm. These were

assigned to the methyl and methylene protons of DSPE (Fig. S3). The chemical shift at 3.63 ppm was assigned to the methylene proton of PEG. The chemical shifts at 6.79 and 7.09 ppm were assigned to the 4-hydroxyphenyl ring protons of the tyrosine, and those between 1.5 to 3 ppm and 4 to 4.5 ppm were assigned to the overlapping proton signals from the peptide and DSPE-PEG segments. <sup>1</sup>H NMR confirmed the presence of both the CCR5-peptide and DSPE-PEG segments, affirming the synthesis of the DSPE-PEG-CCR5. High-resolution mass spectrometry results further supported its synthesis (Fig. S4).

#### LBPN physicochemical properties

LBPNs were prepared using microfluidic techniques that involve the rapid, chaotic mixing of lipid and aqueous phases (Fig. 2B). The LBNP-RPV-CCR5 contained a mixture of PC (45 wt%), DSPE-PEG (19.5 wt%), RPV (35 wt%), and DSPE-PEG-CCR5 (0.5 wt%) in its lipid phase. PBS was used in the aqueous phase (Table 1 and Fig. 2C). LBNP-RPV without DSPE-PEG-CCR5 was prepared in parallel to serve as a control formulation. To track by PET, both LBPNs were reformulated with 1.5 wt%

**Table 1 | The lipid compositions and physicochemical properties of the LBNPs**

Sample	Composition (wt %)	Size <sup>a</sup> (nm)	Zeta <sup>a</sup> potential (mV)	RPV Content <sup>b</sup> (wt %)
LBNP-RPV	PC: 45%, DSPE-PEG:20% and RPV: 35%	98 ± 06	0.29 ± 0.13	49.78
LBNP-RPV-CCR5	PC: 45%, DSPE-PEG:19.5%, RPV: 35% and DSPC-PEG-CCR5: 0.5%	91 ± 14	0.37 ± 0.18	30.80

For the biodistribution study, 1.5 wt% CuInEuS<sub>2</sub> nanoprobe was included in the formulation to track them under positron emission tomography scan.

<sup>a</sup>Evaluated by using dynamic light scattering.

<sup>b</sup>Determined by using mass spectrometry.

of the radioactive nanoprobe <sup>64</sup>CuInEuS<sub>2</sub>. In all other studies, LBNPs were prepared and used without the nanoprobe. TEM images revealed a nearly spherical morphology of both LBNPs (Fig. 3A, B), with representative particles highlighted by red arrowheads. The particle sizes of LBNP-RPV and LBNP-RPV-CCR5 were 98 and 91 nm, respectively (Table 1 and Fig. 3C, D). LBNPs were neutral in charge with a surface zeta potential from 0.29 to 0.37 mV (Table 1). We have used nonionic DSPE-PEG in our formulation to increase the colloidal stability of LBNPs. In biological media, PEG forms a hydration layer around the LBNPs, creating a physical barrier that prevents aggregation and improves their dispersion<sup>18,19</sup>. LBNPs with particle sizes of ~100 nm and a neutral surface charge were well-suited for intravenous administration. The RPV loading content in LBNP-RPV and LBNP-RPV-CCR5 were 49.78 and 30.80 wt%, respectively (Table 1). Moreover, both nanoparticles showed slightly decreased RPV loading content (~4.5 wt%) when co-encapsulated with the nanoprobe (Table S1). Since LBNPs have a constant cargo encapsulating capacity, the co-encapsulation of both the drug and nanoprobe led to the displacement of a portion of the drug to maintain their integrity. This could be the reason for the slight decrease in RPV loading content. Furthermore, both LBNPs displayed a nearly neutral zeta potential and showed a minimal increase in particle size and heterogeneity after nanoprobe incorporation (Table S1 and Fig. S5). Next, the concentration of the CCR5 ligand on the surface of LBNP-RPV-CCR5 was determined using a bicinchoninic acid (BCA) assay. The analysis revealed 3.98 µg of DSPE-PEG-CCR5 peptide ligand per mg of LBNP-RPV-CCR5. Furthermore, the storage stability of the LBNPs was evaluated at 4 °C. LBNPs showed no changes in particle size and dispersity for up to one month, indicating long-term storage stability (Fig. 3E, F).

### LBNP treatment of human monocyte-derived macrophages (MDMs)

Macrophages express CD4 and CCR5 receptors and are susceptible to HIV-1 infection<sup>20–22</sup>. The cells are a known HIV reservoir<sup>23</sup>. Infected macrophages, which can spread the virus throughout the body, also act as reservoirs for ARVs. Therefore, MDM served as a primary cell model to examine the antiretroviral efficacy of LBNP. Before LBNP treatment, the viability of MDMs was evaluated by the CellTiter-Blue Assay with serially diluted LBNPs, ranging from 200 to 3 µM equivalent of RPV (Fig. 4A). The tests revealed >90% MDM viability with a dose equivalent of up to 100 µM RPV. To evaluate LBNP uptake in MDMs, we used 20 µM RPV. The LBNPs showed a time-dependent increase in RPV concentration for up to 12 h, reaching equilibrium between 12 to 24 h (Fig. 4B). LBNP-RPV-CCR5 showed a 3-fold higher RPV uptake at 12 h compared to equivalent LBNP-RPV levels. To test whether cell uptake was CCR5 mediated, comparisons were made with and without the CCR5 antagonist, maraviroc (MVC). With 1 nM/10<sup>6</sup> cell exposures, MVC reduced LBNP-RPV-CCR5 uptake. However, no MVC effect was seen for LBNP-RPV (Fig. 4C). To affirm these results, Cy5.5 dye-labeled LBNPs with equivalent Cy5.5 content were incubated with MDMs with or without MVC. After 4 h, MDMs' nuclei and cell membranes were stained with DAPI (blue, stained DNA) and phalloidin (green, stained F-actin). The microscopic images revealed a bright red fluorescence (Cy5.5) of LBNP-RPV-CCR5 throughout the MDMs (Fig. 4D). However, differential LBNP localization with reduced fluorescence intensity was

observed for MVC treatments. These data affirmed that the entry of LBNP-RPV-CCR5 was blocked by inhibition of the CCR5-receptor. Moreover, MVC did not influence LBNP-RPV uptake. These data affirm that the LBNP-RPV-CCR5 cell entry principally followed a CCR5-receptor-mediated pathway. In addition, MVC treatment did not affect cytotoxicities as it revealed > 90% cell viability at 1 nM treatment dose (Fig. S6). The change in cell morphology in MVC-pretreated MDMs was likely due to the interaction between MVC and the CCR5 cell surface receptor<sup>24</sup>.

To evaluate the RPV retention and viral suppression of the LBNPs, phorbol 12-myristate 13-acetate (PMA) cell stimulation was used to maximize cell differentiation. The fully differentiated PMA-treated cells were then infected with HIV-1<sub>ADA</sub> at the multiplicity of infection (MOI) 0.1 and treated with LBNP-RPV or LBNP-RPV-CCR5 at 100 µM RPV doses. After 24 h, treatment was removed, and cells were cultured in fresh media. Infected MDMs without LBNPs were maintained as controls (HIV-1<sub>ADA</sub> and PMA). On days 1, 5, 9, 15, 21, and 25, culture supernatant fluids were removed and then analyzed for HIV-1 reverse transcriptase (RT) activity. Cells were harvested in parallel to quantify RPV levels. On day 9, LBNP-RPV showed 26 and 5 nmol RPV retention at 100 and 30 µM treatment doses, respectively (Fig. 4E and Fig. S7A). In contrast, LBNP-RPV-CCR5 showed 109 and 50 nmol RPV at 100 and 30 µM treatment doses. Both LBNPs demonstrated a dose-dependent RPV retention. Each showed higher RPV retention at 100 than 30 µM (Fig. 4E and Fig. S7A). In addition, the RPV retention followed descending trends over time throughout the treatment groups. At both doses, LBNP-RPV-CCR5 demonstrated higher RPV retention than LBNP-RPV. These results support the role of the CCR5 receptor in LBNP-RPV-CCR5 cell uptake and its influence on the formation of the macrophage drug depot. To confirm these, LBNP-containing macrophages were examined under TEM. Macrophages showed considerable RPV depots (red arrowhead, Fig. 4F) in LBNP-RPV-CCR5 treated cells than for LBNP-RPV. In parallel tests, HIV-1 RT activity assessed virion production in HIV-1<sub>ADA</sub> infected control groups (Fig. 4G). A single 100 µM dose of LBNP-RPV-CCR5 inhibited virion production for up to 25 days. In contrast, the LBNP-RPV showed viral breakthrough after day 9 (Fig. 4G). The reduced efficacy of LBNP-RPV in inhibiting HIV-1 replication was coordinated to lower RPV retention (5.10 nmol at day 9). The 100 µM dose of LBNP-RPV-CCR5 restricted viral growth for up to 25 days, while the 30 µM dose was unsuccessful (Fig. S7B). At 30 µM of LBNP-RPV-CCR5, the decreased RPV retention (3 nmol at day 25) was insufficient to inhibit viral growth (Fig. S7).

### Biodistribution of LBNPs in hu mice

HIV uses CCR5 as a coreceptor for viral infection. The lack of this receptor in regular mice necessitates using hu mice for HIV infection<sup>25</sup>. Thus, hu mice were used to evaluate the biodistribution of <sup>64</sup>CuInEuS<sub>2</sub> encapsulated theranostic LBNPs. The biodistribution was performed with PET-CT bioimaging. Before bioimaging, we assessed the stability of the radiolabeled LBNPs in mouse plasma which aids in precluding any false positive signals. LBNPs were incubated in 10% human plasma at 37 °C to determine the radiolabeling stability. The radioactivity in the LBNP was measured in relation to the total radioactivity of the LBNP plasma solution. The radiolabeled NPs were stable (98%, Fig. S8) in mouse plasma after 24 h of incubation. This result was further

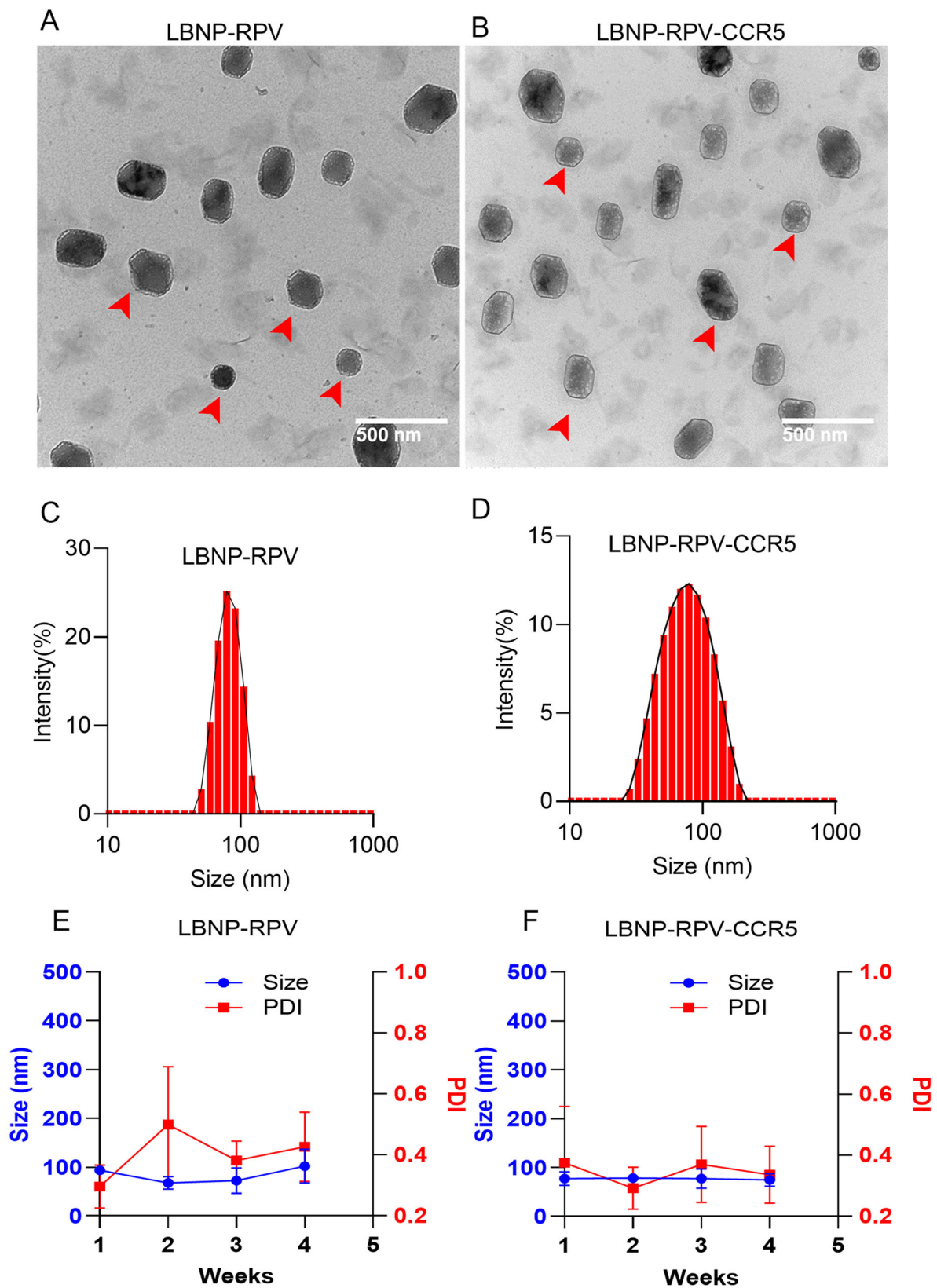
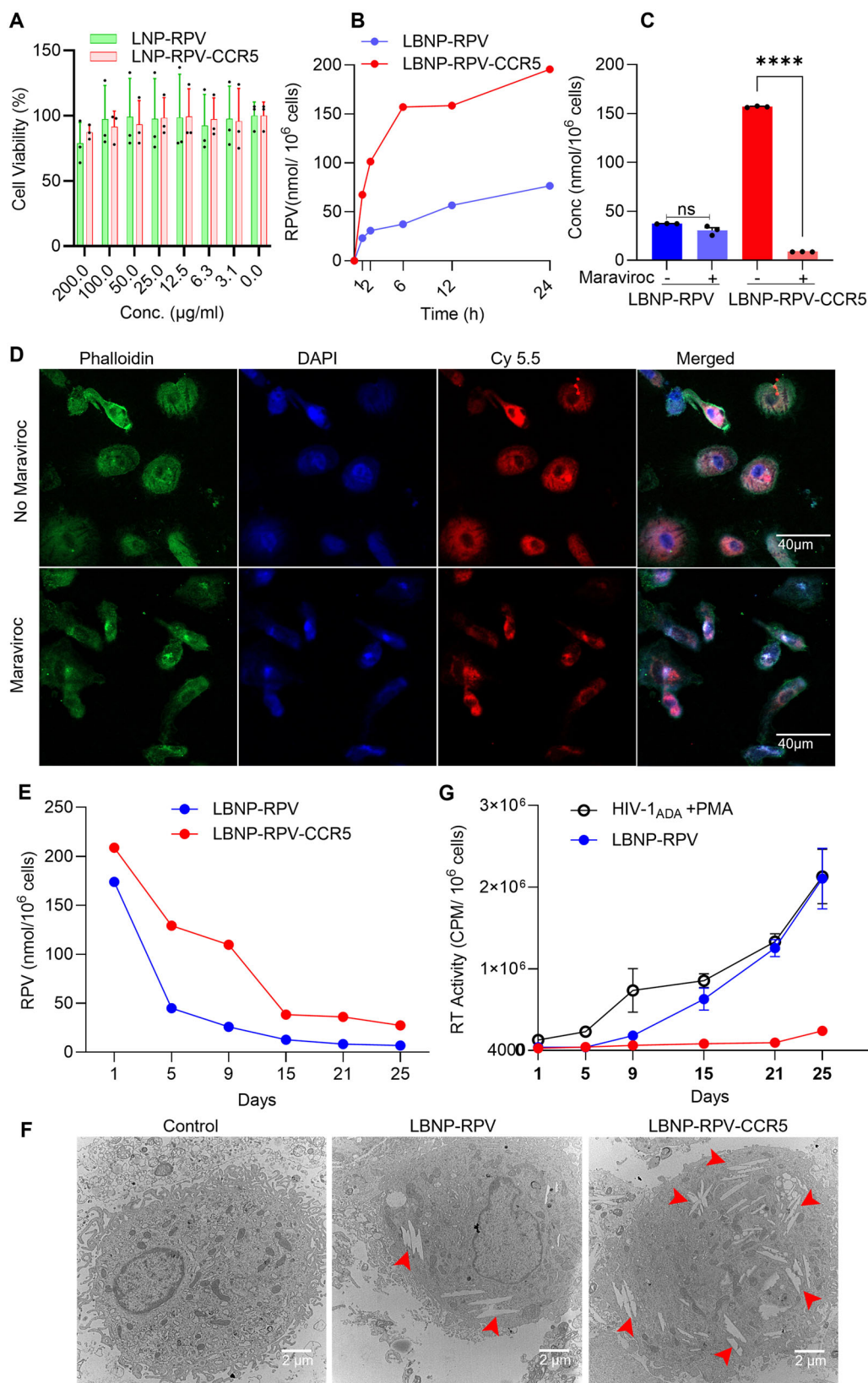


**Fig. 3 | Physicochemical LBNP characterization.** **A, B** The TEM image shows a spherical LBNP-RPV and LBNP-RPV-CCR5 morphology. The red arrowheads were used to indicate the representative particles. **C, D** The DLS size profile demonstrates the unimodal distribution of the LBNPs. **E, F** The changes in size and

polydispersity of the LBNPs were recorded for one month at 4 °C. LBNPs were stable without changes in size and polydispersity. Results are expressed as the mean  $\pm$  SD for independent replicates ( $n = 3$ ).



supported by quantifying nearly similar levels of RPV in both the LBNP and LBNP-plasma solutions after 24 h of incubation (Fig. S8). Collectively, these sets of experiments suggested their suitability for *in vivo* bioimaging and drug delivery. Radiolabeled LBNPs (dose 1000  $\mu\text{Ci}/\text{kg}$ ) were injected by tail vein to hu mice to assess particle biodistribution<sup>26</sup>. It is important to clarify that the nanoprobe was used exclusively for

PET imaging, while the rest of the study was conducted without it. PET images were captured at 6, 24, and 48 h after injection and co-registered by CT (Fig. 5A–E). Both the coronal and sagittal PET-CT images demonstrated spleen and liver LBNP distribution (Fig. 5B). The PET image displayed a progressive decrease of radioactive signals over time. This was attributed to the combined effect of radioactive decay

**Fig. 4 | CCR5-receptor-induced LBNPs uptake, depot formation and HIV-1 viral suppression in MDMs, Ex-vivo.** **A** Dose-associated macrophage viability measurements following LBNP exposures by the CTB assay after 24 h incubation. Both the LBNP-RPV and LBNP-RPV-CCR5 showed cell viability above 90% up to 100  $\mu$ M RPV concentration. **B** LBNP-RPV and LBNP-RPV-CCR5 macrophage uptake was analyzed by measuring RPV concentration for 24 h at 20  $\mu$ M RPV. LBNP-RPV-CCR5 showed a 3-fold increase in drug uptake than LBNP-RPV. **C** The CCR5 inhibitor (maraviroc, 1 nM) attenuated the uptake of LBNP-RPV-CCR5. **D** Confocal microscopy was performed with Cy5.5 dye-labeled LBNP-RPV-CCR5 treated macrophages in the presence (lower panel) and absence (upper panel) of maraviroc. The nuclei and cell membranes were stained with DAPI (blue, stained DNA) and phalloidin

(green, stained F-actin), respectively. **E** RPV retention was evaluated by measuring RPV in the cell supernatant fluids. **F** TEM image of LBNP engulfed macrophage. Macrophages show multiple depots in LBNP-RPV-CCR5 than in LBNP-RPV as highlighted by red arrowhead. **G** The viral suppression in LBNP-RPV and LBNP-RPV-CCR5 treated macrophages was evaluated by measuring virus levels in the cell supernatant fluids. The data were collected over 25 days after a 100  $\mu$ M administered dose. The reproducibility of cellular uptake and depot formation were verified by at least 3 independent experiments. All results are expressed as the mean  $\pm$  SD for  $n = 3$  biological replicates. Statistical analysis was performed by an unpaired t-test. \*\*\*\*,  $P < 0.0001$ ; and ns = not significant.

and LBNP excretion<sup>27</sup>. Noticeably, LBNP-RPV-CCR5 showed primary presence in the spleen, while LBNP-RPV primarily accumulated in the liver. Comprehensively, the higher signal in LBNP-RPV-CCR5 treated mice over LBNP-RPV was linked to its minimal injection site (tail vein) aggregation (Fig. S9). To validate these findings, mice were sacrificed 48 h after injection, and the remaining radioactivity was assayed by a gamma counter (Fig. 5C, D). LBNP-RPV-CCR5 showed a propensity to spleen tissue accumulation. In contrast, LBNP-RPV was distributed throughout all examined tissues. LBNP-RPV-CCR5 showed a substantially higher spleen/liver radioactivity ratio than LBNP-RPV. This increased spleen accumulation was likely due to the high number of CCR5-expressing immunocytes in the spleen<sup>28</sup>.

To evaluate RPV distribution, LBNP-RPV and LBNP-RPV-CCR5 were injected with 25 mg/kg RPV dose through the tail vein of the hu mice. The plasma RPV concentration was measured 6 and 24 h after injection (Fig. 5F, G). At 24 h, mice were sacrificed, and the liver, spleen, and other tissue RPV levels were determined by electrospray ionization mass spectrometry (Fig. S10). At 24 h, plasma, liver, and spleen RPV levels were  $120 \pm 38$ ,  $4081 \pm 473$ , and  $4600 \pm 217$  ng/g, respectively, in LBNP-RPV-CCR5 treated mice. In contrast, RPV levels were  $299 \pm 32$ ,  $2919 \pm 447$ , and  $1898 \pm 352$  ng/g in the LBNP-RPV control mice. LBNP-RPV-CCR5 demonstrated spleen-specific RPV accumulation with higher spleen/liver RPV ratios than LBNP-RPV (Fig. 5H). The slight discrepancies in the correlation between tissue RPV distribution (Fig. 5F–H, Fig. S10) and PET imaging (Fig. 5B–E) arose because the PET imaging was conducted with the nanoprobe, while RPV distribution studies did not require it. Since the incorporation of the nanoprobe did not significantly affect the morphology and surface charge of the LBNPs (Table S1 and Fig. S5), the discrepancies may have stemmed from variations in plasma protein corona formation associated with the presence or absence of the nanoprobe in the LBNPs<sup>29,30</sup>. This variation may eventually have influenced the tissue distribution of the LBNPs with and without the nanoprobe. However, both experiments confirmed that LBNP-RPV-CCR5 accumulated to a more significant level in the spleen compared to LBNP-RPV.

Yet another limitation of ARV biodistribution rests in penetrance to the brain viral sanctuary. Although some reports suggest that CCR5 ligand can enhance BBB penetration in vitro, the BBB in live mice is significantly more complex<sup>31</sup>. However, predicting the in vivo performance of CCR5 ligands based on laboratory assays is challenging. Moreover, the delivery of LBNP-RPV-CCR5 is limited by its poor ability to cross the blood-brain barrier (BBB). This is evidenced by the undetectable brain signal in in vivo imaging system (IVIS) and the low levels of RPV when BBB opening is not facilitated by focused ultrasound (FUS) (Fig. 6A, B and D). To enhance LBNP penetration into the brain, we used FUS with microbubble-induced BBB disruption (BBBd) in our hu mice (Fig. 6A). The verification of BBBd was affirmed by the gadolinium enhancements MRI, which displayed bright signals (indicated by blue arrows) in the coronal sections of the T1-weighted images (TIWI) (Fig. 6C). Furthermore, susceptibility-weighted imaging (SWI) did not reveal any evidence of microhemorrhages (Fig. 6C). Immediately following the tail vein injection of microbubbles and FUS, mice were intravenously injected with Cy5.5 labeled LBNPs. The FUS-

mediated transient BBB disruption allows the LBNP to cross into the brain. After FUS, the BBB naturally reseals; a similar strategy can be applied to humans<sup>32</sup>. On the following day, whole-body scans were performed with an IVIS. This revealed a higher brain accumulation and retention of LBNP-RPV-CCR5 than LBNP-RPV (Fig. 6B). This data was affirmed by quantifying the elevated levels of RPV in brain tissue by mass spectrometry. Specifically, the brain tissue of the LBNP-RPV-CCR5 treated hu mice showed RPV levels of  $400.5 \pm 7.5$  ng/g, compared to  $55.3 \pm 9.8$  ng/g in those treated with LBNP-RPV. Although FUS-mediated BBB disruption facilitates the delivery of both LBNPs to the brain, LBNP-RPV-CCR5 showed the highest retention based on its interactions with CCR5 receptor-expressing human myeloid-microglial cells<sup>33</sup>. To examine cell-specificity, brain tissue sections were stained with IBA-1 (red, microglia) and HuNu (green, human nuclei) and imaged by fluorescence microscopy (Fig. 6E). Approximately 50% of microglia (IBA-1, red) showed HuNu, green staining, and LBNP engulfment. Mice treated with LBNP-RPV-CCR5 displayed increased accumulation of LBNPs in human microglia and higher cytoplasmic retention than those treated with LBNP-RPV (Fig. 6F). These data support CCR5 targeted delivery.

### LBNP-RPV-CCR5 viral suppression in hu mice

After achieving higher levels of viral suppression in MDMs and lymphoid tissue-specific RPV biodistribution in human cell reconstituted hu mice, an animal study was designed to validate levels of viral suppression for the LBNP-RPV-CCR5. The timeline of the experiment is presented in Fig. 7A. Hu mice were infected with  $1.5 \times 10^4$  tissue culture infectious dose 50 (TCID<sub>50</sub>) of HIV-1<sub>ADA</sub>. At two weeks, viral replication was confirmed by measuring plasma viral RNA copies. Subsequently, LBNPs were administered by the tail vein injection at a dose of 25 mg/kg RPV equivalence. Viral suppression efficacy was analyzed by weekly plasma viral load measurements. Levels of viral suppression compared against LBNP-RPV and LBNP-RPV-CCR5, the latter successfully held viral growth for 14 days in 2/3 treated mice (Fig. 7B). To evaluate viral suppression at the tissue level, we conducted immunohistochemical staining for the HIV-1 p24 antigen in the spleen, liver, lung, heart, and kidney (Figs. S11 and S13A). The results revealed a significant presence of HIV-1-positive cells in the spleen and liver of the LBNP untreated group. We observed a decreasing trend in HIV-1 positive cells from the LBNP-RPV group to the LBNP-RPV-CCR5 group, indicating that the LBNP-RPV-CCR5 treatment provided improved viral suppression. Additionally, to assess viral suppression in microglial cells, we stained brain tissues with IBA-1 (for microglia), DAPI (for nuclei), and HIV-1 p24 (for the p24 antigen) (Figs. S12 and S13B). The staining results showed a significant reduction in HIV-1 p24 intensity in the LBNP-RPV-CCR5 group compared to the LBNP-RPV group, suggesting that the LBNP-RPV-CCR5 treatment is more effective at reducing viral load in the microglial cells. The higher levels of viral suppression of LBNP-RPV-CCR5 were linked to CCR5-receptor-mediated lymphoid-specific RPV retention.

### Tissue toxicity measurements

To assess the potential toxicity of LBNP, the body weight of the hu mice was measured. Blood samples were collected to determine

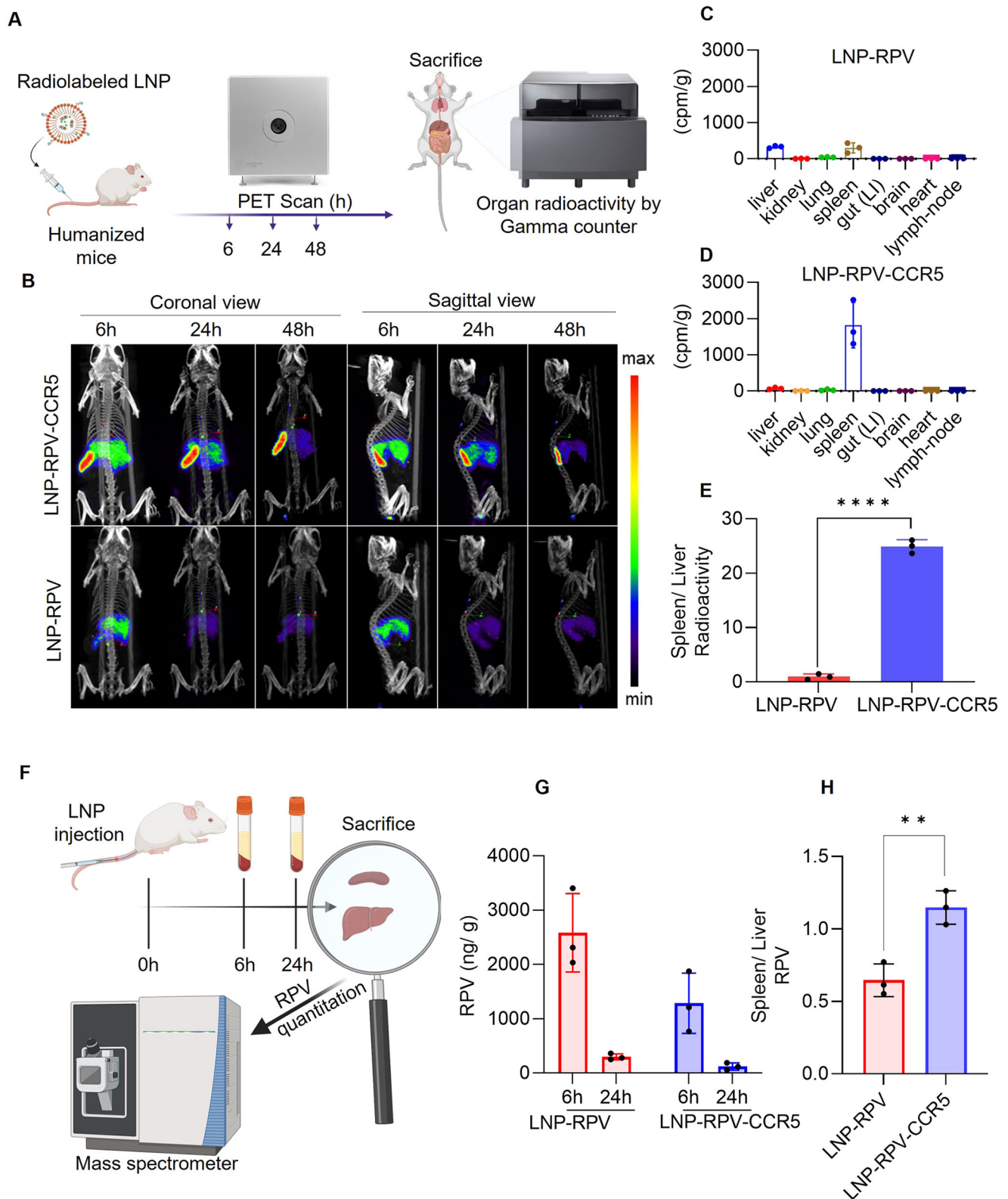


**Fig. 5 | LBNP and RPV tissue biodistribution in mice by PET imaging and mass spectrometry.** **A** Schematic presentation of LBNP biodistribution by PET. **B** Humanized mice were injected with LBNP-RPV or LBNP-RPV-CCR5, and particle biodistribution was monitored by PET at 6, 24, and 48 h. Both coronal (left panel) and sagittal (right panel) views of mice are illustrated. **C, D** Quantitative measurements of radiolabeled LBNPs in tissue were recorded at 48 h post-administration by using a gamma counter. LBNP-RPV-CCR5 was concentrated in the spleen. **E** Spleen/liver radioactivity ratios for LBNP-RPV-CCR5 and LBNP-RPV are shown. **F A**

schematic presentation of LBNP injection and RPV quantitation in humanized mice is shown. **G** Plasma RPV levels in mice treated with LBNP-RPV and LBNP-RPV-CCR5 are shown at 6 and 24 h post-injection. **H** The spleen/liver RPV ratio at 24 h post-injection of LBNPs. The results presented in Figures A to E were obtained with nanoprobe-containing LBNPs, whereas those in Figures F to H were acquired using LBNPs without the nanoprobe. Figures A and F were created in BioRender<sup>35</sup>. Results are presented as the mean  $\pm$  SD for  $n = 3$  biological replicates. Statistical significance was calculated by using an unpaired t-test, \*\* $P < 0.01$ , and \*\*\*\* $P < 0.0001$ .



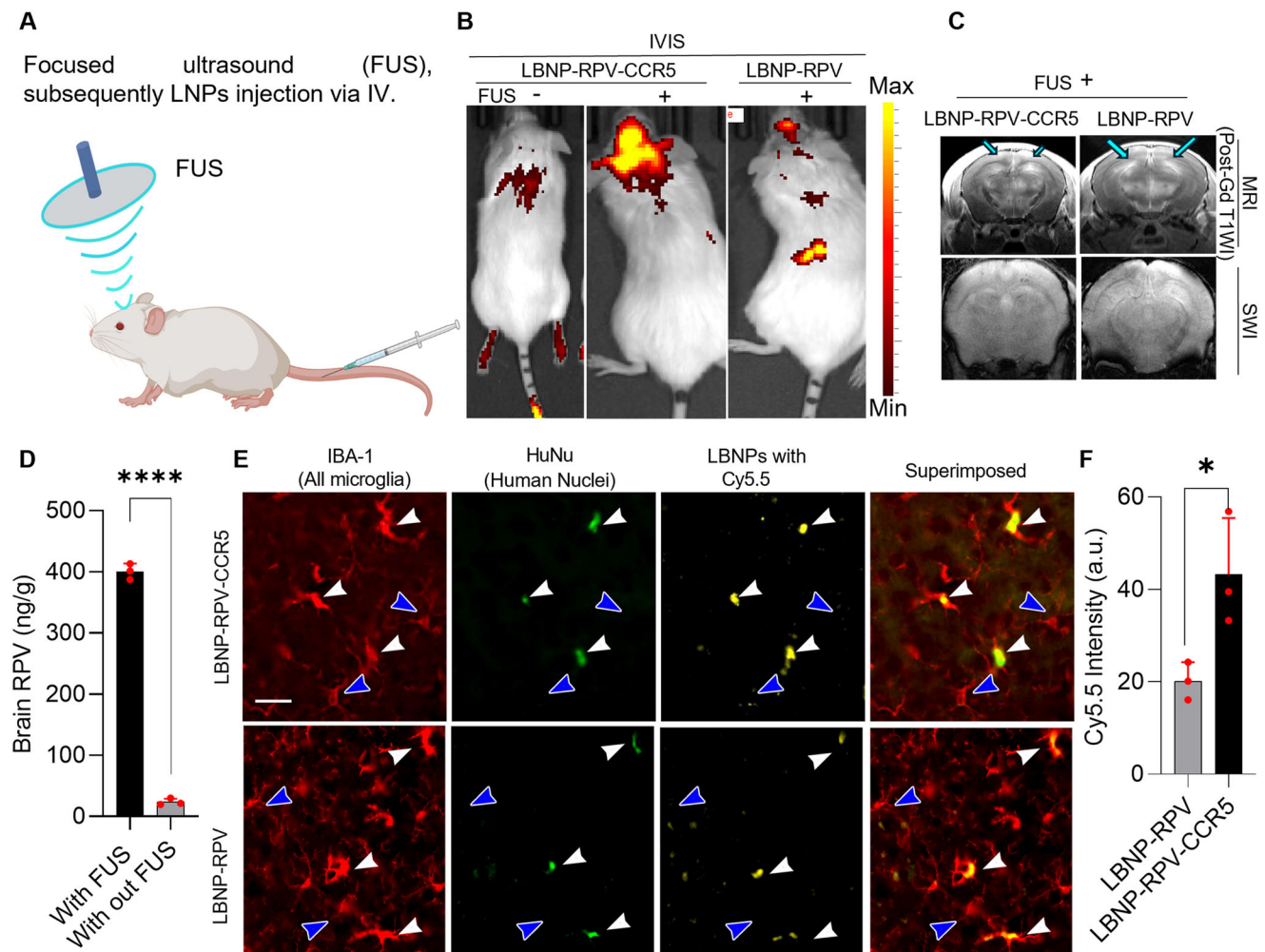


**Fig. 6 | Brain delivery of LBNP-RPV-CCR5 nanoparticles.** **A** Schematic presentation of FUS-treated humanized microglial (MG) mice that received LBNP treatment, created in BioRender<sup>35</sup>. **B** IVIS images show bright yellow Cy5.5 signals in the brains of FUS-treated mice (middle) that received LBNP-RPV-CCR5, compared to those without FUS treatment (left). With FUS treatment, the mice receiving LBNP-RPV-CCR5 (middle) show higher brain accumulation than those receiving LBNP-RPV (right). **C** Both mice showed good BBB disruption, as shown by the gadolinium enhancements (bright signals, blue arrows) on the coronal sections of the T1-weighted images (T1WI) on MRI. The susceptibility-weighted imaging (SWI) revealed the absence of microhemorrhages. **D** The brain RPV level in LBNP-RPV-CCR5 treated mice with and without FUS. **E** The fluorescence microscopy image of brain tissue sections, stained with IBA-1 (red, microglia) and HuNu (green, human

nuclei). Approximately 50% of microglia (IBA-1, red stain) in the hu mice were positive for the human marker (HuNu, green stain, white arrows), while mouse microglia are not immunoreactive to HuNu (blue arrows). Both the LBNP-RPV and LBNP-RPV-CCR5 treated mice show Cy5.5 signals in the brain tissue; however, only the microglia with the HuNu stains showed engulfment of the LBNPs as the Cy5.5 signals appeared in the cytoplasm of the human microglia (white arrows). **F** Quantification of Cy5.5 signal intensity from fluorescence microscopy images of brain tissue, analyzed using ImageJ. Furthermore, the Cy5.5 signals appear to be more intense in the animals that received the LBNP-RPV-CCR5 than LBNP-RPV. Scale bar = 25  $\mu\text{m}$ . All results are expressed as the mean  $\pm$  SD for  $n = 3$  biological replicates. Statistical significance was calculated using an unpaired t-test, \* $P < 0.05$  and \*\*\*\* $P < 0.0001$ .

hematologic profiles at the end of treatment. The heart, lung, spleen, liver, and kidneys were paraformaldehyde-fixed, sectioned, and stained with hematoxylin and eosin to assess tissue histology. The analysis of whole blood counts and blood serum chemistry revealed no evidence of cytotoxicity in the LBNP-treated group (Tables S2 and S3). Moreover, the measured body weight remained unchanged throughout all the treatments (Fig. 7C). No histological abnormalities were identified in the spleen despite the high levels of LBNP accumulation and in other examined organs (Fig. 7D). These limited examinations indicate that the LBNPs were safe delivery vehicles. The results of these studies support the clinical translation of the LBNP-based drug delivery.

In conclusion, we successfully synthesized a multimodal radioactive nanoprobe with a CCR5-peptide conjugated DSPE-PEG-CCR5 lipid. The CCR5-targeted LBNP-RPV-CCR5 and nontargeted LBNP-RPV were formulated by microfluidic mixing. The spherically shaped LBNPs

had sizes near 100 nm with narrow size dispersity. These LBNPs were devoid of associated toxicities at 100  $\mu\text{M}$  RPV equivalent doses. Unlike LBNP-RPV, LBNP-RPV-CCR5 demonstrated substantially higher macrophage uptake and retention. In macrophages, the RPV was retained as a drug depot. A single dose of LBNP-RPV-CCR5 treatment demonstrated a 25-day-long viral suppression in the HIV-1 infected macrophages, not seen by LBNP-RPV treatments. The CCR5-receptor-mediated RPV uptake and extended drug persistence were linked to extended viral suppression. The PET-CT theranostic imaging revealed a spleen-specific biodistribution of LBNP-RPV-CCR5, resulting in a higher RPV accumulation in the spleen of hu mice, a key HIV reservoir. The FUS combined with microbubble-induced BBBd facilitated the delivery of LBNPs to the brain and higher retention in human microglia. Moreover, a single dose of LBNP-RPV-CCR5 was sufficient to hold viral growth at bay in HIV-1 infected hu mice. The therapeutic efficacy of the CCR5-receptor targeted delivery system can be propelled by a

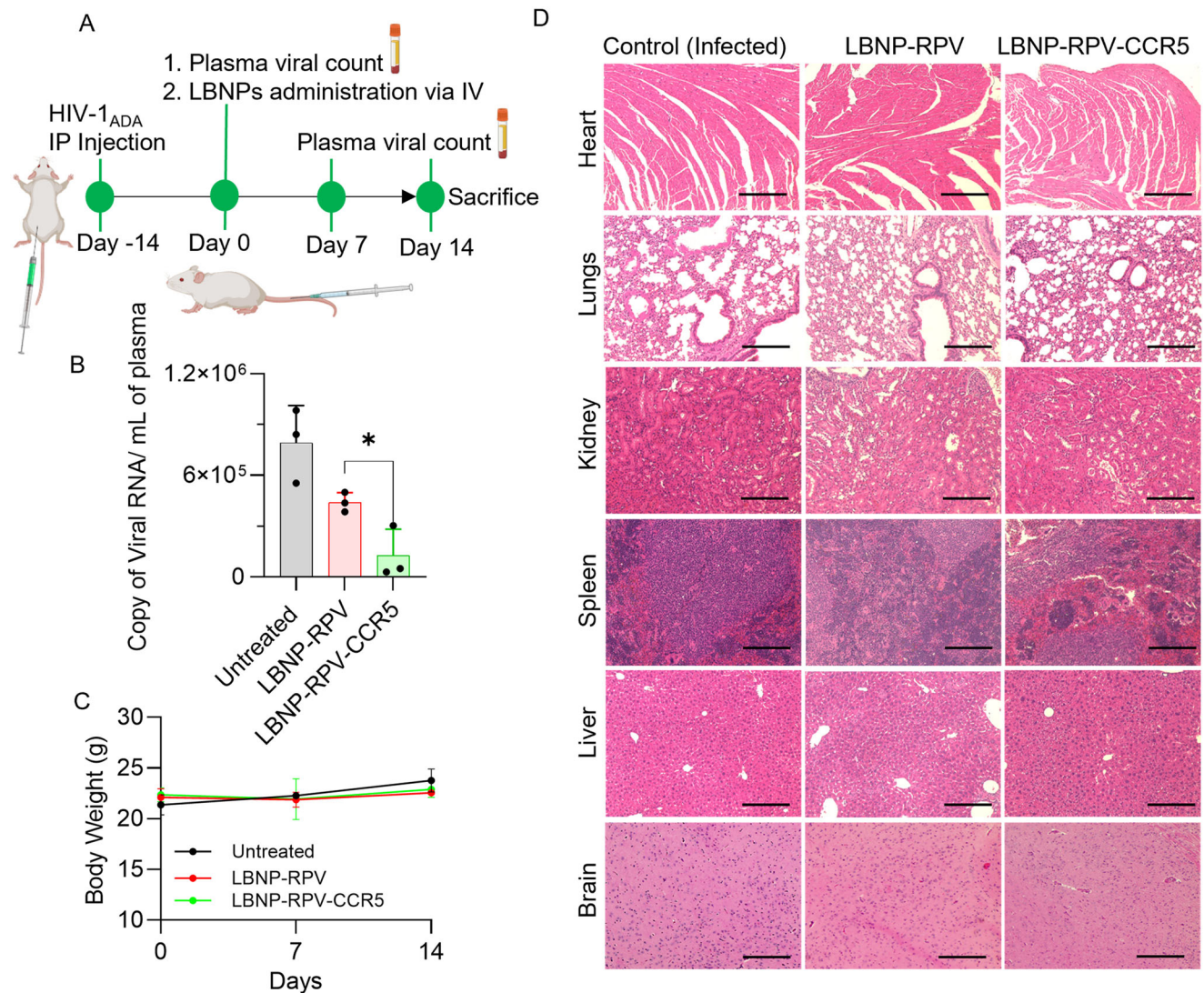


**Fig. 7 | Viral suppression and toxicity profiles of RPV-encapsulated LBNP.**

**A** Schematic representations of experimental profiles of LBNP treatments, Created in BioRender<sup>35</sup>. **B** Viral suppression efficiency of LBNP-RPV and LBNP-RPV-CCR5 on day 14 are illustrated. LBNP-RPV-CCR5 showed complete viral suppression in 2/3 of the treated mice up to day 14 (number animals  $n = 3$  per group). **C** The change in mice body weight in the untreated, LBNP-RPV, and LBNP-

RPV-CCR5 treated group. **D** The histological images of hematoxylin and eosin-stained heart, lung, kidney, spleen, liver, and brain tissue sections from the treatment groups. The images were captured at 20X magnification (Scale bar 200 μm). All results are expressed as the mean ± SD for  $n = 3$  biological replicates. Statistical significance was calculated using an unpaired t-test, \* $P < 0.05$ .

synergistic combination of multiple ARVs for longer-term effective HIV-1 treatments.

## Methods

### Materials

Copper (II) chloride dihydrate (307483), Indium (III) chloride (334065), Europium (III) chloride hexahydrate (203254), Thioacetamide (163678), Oleic acid (364525), Oleylamine (969831), 1-octadecene (O806-1L), L- $\alpha$ -phosphatidylcholine (PC) (from egg yolk), 3-(4,5-dimethylthiazol-2-yl)-2,5-diphenyltetrazolium bromide (MTT), were obtained from Sigma Aldrich, St. Louis, MO, USA. Phorbol 12-myristate 13-acetate (PMA; P8138), 1-octanol, paraformaldehyde (PFA), were obtained from Sigma Aldrich (St. Louis, MO, USA). Dulbecco's modified eagle's medium (DMEM) containing glucose (4.5 g/L), phosphate-buffered saline (PBS), gentamicin, L-glutamine, sodium pyruvate, AcroMetrix EDTA Plasma Dilution Matrix (S2284) were purchased from Thermo Fisher Scientific/Gibco (Waltham, MA, USA). Heat-inactivated pooled human serum was purchased from Innovative Biologics (Herndon, VA). Cell Titer Blue™ (CTB; G8080) was purchased from

Promega (Madison, WI, USA). Rilpivirine (RPV; A904176) was purchased from Amadis Chemical (Zhejiang, China). 1,20-distearoylphosphatidylethanolaminemethyl-polyethyleneglycol conjugate 2000 (DSPE-PEG2000), DSPE-PEG<sub>2000</sub> carboxy NHS and DSPE-PEG(2000)-N-Cy5.5 were purchased from Avanti Polar Lipids (Birmingham, AL, USA). The CCR5 targeting peptide, D-Ala-Ser-Thr-Thr-Thr-Asn-Tyr-Thr-NH<sub>2</sub> was purchased from P3 BioSystems (Louisville, KY, USA). The radioactive 64 copper chloride (<sup>64</sup>CuCl<sub>2</sub>) was requested and delivered from the Washington University School of Medicine MIR cyclotron facility (St. Louis, MO, USA).

### Synthesis of radioactive nanoprobes

The multimodal nanoprobe particles were prepared by the solvothermal method. At first, the thioacetamide (15.026 mg, 2 mmol) and oleylamine (6 mL) were taken in a 20 mL glass vial, and the reaction mixture was sonicated for 2 min (operated at 20%, Cole-Parmer 750 W model CPX750, IL, USA). In a separate vial, indium (III) chloride dihydrate (22.118 mg, 1 mmol), europium (III) chloride hexahydrate (36.64 mg, 1 mmol), 1-octadecene (10 mL), and oleic acid (6 mL) were

homogenized by vigorous stirring. The homogeneous solution was transferred to the reaction mixture and further probe sonicated for 5 min. Subsequently, the copper (II) chloride dihydrate (34.09 mg, 2 mmol) was also added to the reaction mixture. The reaction mixture was quickly transferred to the Teflon-lined hydrothermal autoclave and heated at 280 °C for 8 h. After the autoclave cooled down to room temperature, the crude reaction mixture was dispersed in ethanol (50 mL) by sonication. The solution was then spun down (950 × *g* for 30 minutes at 20 °C) and decanted off the supernatant. This ethanol-washing step was repeated thrice to remove unreacted starting materials. The particles were then stored in a desiccator for future use. To make the radioactive nanoprobe, the copper (II) chloride was substituted with radioactive copper (II)-64 chloride.

The bulk morphology and crystal lattice structure of the CuInEuS<sub>2</sub> nanoprobe were characterized by high-resolution transmission electron microscopy and selected area electron diffraction, respectively. The elemental composition and chemical color mapping were analyzed by energy-dispersive X-ray spectroscopy and scanning transmission electron microscopy scanning (STEM) with high-angle annular dark-field (HAADF) (FEI Tecnai Osiris S/TEM operated at 200 kV), respectively. The nanoprobe's surface composition and crystal structure were analyzed by XPS (Thermo Fisher Scientific, Waltham, MA, USA) and powder XRD (Rigaku SmartLab Diffractometer, Rigaku Corporation, Tokyo, Japan). The thermal property was analyzed by differential scanning calorimetry (NETZSCH DSC 204 F1 Phoenix, Waldkraiburg, Bayern, Germany) and thermogravimetric analysis (NETZSCH TGA 209 F1 Libra system, Waldkraiburg, Bayern, Germany).

### Synthesis of CCR5 targeting peptide conjugated DSPE-PEG-CCR5 formulations

A linear peptide with a sequence of D-Ala-Ser-Thr-Thr-Thr-Asn-Tyr-Thr-NH<sub>2</sub> has been selected as a CCR5-receptor targeting ligand. The free amine group of the peptide was conjugated with PEG lipid, DSPE-PEG<sub>2000</sub> carboxy NHS via an activated acid-amine coupling reaction. The reaction was conducted in a Schlenk tube by dissolving the peptide (3.57 mg, 4.15 μmol) in anhydrous DMSO (250 μL) followed by the addition of DIPA (10 μL). After 30 min of reaction at room temperature, DMSO dissolved DSPE-PEG<sub>2000</sub> carboxy NHS (10 mg, 3.47 μmol) was added to the reaction mixture and allowed to stir for the next 24 h. The completion of the reaction was examined by thin-layer chromatography using 1:5 (v/v) MeOH/DCM as eluent. After the completion, the crude reaction mixture was dialyzed (cellulose acetate, MWCO 3.5 kDa) against deionized water (DI) to remove the unconjugated peptide. The lyophilization of the dialyzed product ensued in a floppy white solid, further characterized by <sup>1</sup>H NMR spectroscopy.

### LBNPs formulation and their physicochemical properties

LBNPs were formulated by rapidly mixing the lipid and aqueous phases in the microfluidic device. To formulate CCR5-targeted and RPV-encapsulated LBNPs (LBNP-RPV-CCR5), L-α-phosphatidylcholine (PC, 45 wt%), DSPE-PEG2000 (17.5 wt%), RPV (37 wt%), and DSPE-PEG-CCR5 (0.5 wt%) were combined in lipid phase and performed the microfluidization (Precision Nanosystem) with PBS as an aqueous phase (Table 1). The LBNP without CCR5 ligand (LBNP-RPV) was also formulated and used as a control in various experiments. The existing lipid phase was combined with 1.5 wt% of <sup>64</sup>CuInEuS<sub>2</sub> to formulate radiolabel LBNP and 0.5 wt% of DSPE PEG(2000)-N-Cy5.5 lipid to formulate Cy5.5-dye-labeled LBNPs. During LBNP formulation, the ratio of the aqueous phase to the lipid phase was maintained at 3:1 (v/v), and the total flow rate was held at 12 mL/min. After microfluidization, the LBNPs were purified by dialyzing (3.5–5 kDa cut off, cellulose acetate) against PBS over two days. The purified LBNP was further passed through a 40 μm cell strainer to remove the unencapsulated drug precipitate. The LBNPs were sterilized by passing them through a 0.22 μm syringe filter. The size and zeta potential of LBNP were

measured by DLS (Zetasizer Nano ZS, Malvern). The long-term stability of LBNP at 4 °C was evaluated by intermittently measuring their size and zeta potential over a month. The radioactivity of nanoprobe <sup>64</sup>CuInEuS<sub>2</sub> was measured by gamma-ray scintillation spectrometry. (Hidex AMG). To assess the RPV content, the LBNPs (50 μL) were sonicated with methanol (250 μL) for 30 min and subjected to ultra-high performing liquid chromatography (UPLC, Acquity UPLC H-class® system, Waters Milford, MA, USA). Correspondingly, the Cy5.5-lipid content in the LBNP was calculated by measuring the fluorescence (Ex/Em = 683/703 nm) using a benchtop plate reader (Molecular Devices, SpectraMax M3, Sunnyvale, CA). The bulk morphology of the LBNPs was captured under the transmission electron microscope (TEM, FEI Tecnai G2 Spirit TWIN microscope, USA). To determine the drug loading content (LC), a known volume of LBNP solution was lyophilized and the total mass content (drug + lipid) per mL of LBNP was evaluated. The LC was determined by following the equation, (RPV per mL × 100)/ total mass of the LBNP per mL. The BCA assay was conducted to quantify the CCR5 peptide on the surface of LBNP-RPV-CCR5. The DSPE-PEG-CCR5 peptide conjugate was used to generate the standard curve, and LBNP-RPV without the DSPE-PEG-CCR5 peptide served as the control. The amount of CCR5 peptide per milligram of LBNP-RPV-CCR5 was determined by calculating the quantity of the peptide using the BCA assay and considering the total mass of the nanoparticle.

### Plasma stability of radiolabeled LBNPs

The stability of the radiolabeled LBNPs was determined by incubating them in 10% mouse plasma at 37 °C for 24 h. After the incubation, the LBNP-plasma solution's total radioactivity was determined by gamma counter. To measure the radioactivity outside the LBNP, the LBNP-plasma solution was filtered by using centrifugal filtration (Amicon<sup>®</sup>, 10 K molecular-weight cut-off) at 2000 × *g* for 15 min and measured the radioactivity in the filtrate. The percent of radiolabeling stability was determined by using Eq-1.

$$\text{Radiolabeling stability(\%)} = \frac{A - B}{A} \times 100 \quad (1)$$

A=Total radioactivity B=Radioactivity in the filtrate

### Plasma stability of RPV loaded LBNPs

To assess the plasma stability of the RPV-loaded LBNP, the samples were incubated with 10% mouse plasma at 37 °C for 24 h. Following the incubation, the total RPV content in the LBNP-plasma solution was analyzed using mass spectrometry. The solution was then filtered through centrifugal filtration (Amicon<sup>®</sup>, 10 K molecular-weight cut-off) at 2000 × *g* for 15 minutes. The RPV content was quantified in both the pellet and the filtrate via mass spectrometry. RPV encapsulation stability was calculated using Eq-2.

$$\text{RPV encapsulation stability(\%)} = \frac{C - D}{C} \times 100 \quad (2)$$

C=Total RPVD = RPV in the filtrate

### Cell cultures

Monocytes were obtained by leukapheresis from HIV and hepatitis B seronegative donors<sup>34</sup>. The donors were specifically selected and consented to participate, with all procedures approved by the institutional review board (IRB; protocol no. 4017-22-FB) at the University of Nebraska Medical Center. Monocytes were cultured in 10% human serum (heat-inactivated) supplemented Dulbecco's modified Eagle medium (DMEM) containing glucose (4.5 g/L), L-glutamine (200 mM), sodium pyruvate (1 mM), gentamicin (50 μg/mL), ciprofloxacin (10 μg/mL) and recombinant human macrophage colony-stimulating

factor (1000 U/mL) at 37 °C in 5% CO<sub>2</sub> incubator. On every other day, half of the culture media was replaced with fresh media and continued for one week to facilitate MDMs. The MDMs were then incubated with PMA (50 ng/mL) containing media for 24 h and used for ex vivo assays.

### Cell viability assay

The effect of LBNPs on MDM cell viability was evaluated by Cell Titer Blue™ (CTB) assay. MDM containing 96 well plates (1.5 × 10<sup>5</sup> cells/well) were incubated with LBNPs at a dose ranging from 3 to 200 μM equivalent to RPV for 24 h. After the allotted time, the cells were further incubated with CTB solution (20 μL/well) at 37 °C for 2 h, and fluorescence (E<sub>x</sub>/E<sub>m</sub> = 560/590 nm) intensity was recorded on bench top plate reader (Molecular Devices SpectraMax M3, SoftMax Pro 6.2 software). The percentage of cell viability in the treatment group was evaluated by comparing their fluorescence intensity with that of the untreated group. Analogously, the MDM cell viability against MVC was evaluated at a dose ranging from 0.5 to 4 nM.

### LBNP MDM uptake

To evaluate the uptake, LBNPs at doses equivalent to 30 and 100 μM RPV were incubated with MDMs in a 12-well plate (1.0 × 10<sup>6</sup> cells/well) with and without the pretreatment of MVC (1 nM). The uptake of LBNP was determined by the means of RPV uptake. The concentration of RPV in MDMs was measured at 1, 2, 6, 12, and 24 h of post incubation. At each time point, MDMs were washed and scraped with PBS. The scraped cells were pelleted down by centrifugation and sonicated with HPLC-grade methanol (200 μL) to extract the RPV. To remove the cell debris, the methanol solution was further centrifuged (at 5000×g for 10 min), and the supernatant was used to measure RPV concentration by UPLC.

### Antiretroviral activity and LBNP RPV macrophage retention

HIV-1 RT activity was employed to determine the antiretroviral efficacy. MDMs were challenged with HIV-1<sub>ADA</sub> (1.5 × 10<sup>4</sup> TCID<sub>50</sub>/mL) at 0.1 MOI for 8 h. The cells were then washed with PBS and cultured overnight in fresh media. On the following day, HIV-1 infected cells were treated with LBNPs at the dosage of 30 and 100 μM RPV equivalent for 24 h. The treatment was then removed by PBS wash, and the cells were cultured in fresh media. At 1, 5, 9, 15, 21, and 25 days of post-treatment removal, culture media were collected to analyze the RT activity and the associated cells were harvested to quantitate RPV retention.

### Animals

NSG (NOD.Cg-Prkdc<sup>scid</sup> Il2rg<sup>tm1Sug</sup>Tg(CMV-IL34)) mice were obtained from the Jackson Laboratories, Bar Harbor, ME, and bred under specific pathogen-free conditions. All animal studies were reviewed and approved by the IACUC (protocol no 18-110-08) at the University of Nebraska Medical Center by the ethical guidelines set forth by the National Institutes of Health for the care of laboratory animals. Mice were kept in a holding room at 20 °C with 50% humidity and 12 h light/dark cycles. The mice were humanized (hu mice) by following the previously published protocol<sup>13</sup>. Humanization was confirmed by flow cytometry analysis of blood immune cells (CD45 and CD3) staining. At the age of 20 weeks, mice were subjected to the study with 3 mice per group. Sex was not considered in this study because the focus was on LBNP-mediated plasma viral load suppression, which was not expected to differ between male and female mice.

### LBNP biodistribution

PET imaging was performed on hu mice to assess the real-time biodistribution of radio-labeled (<sup>64</sup>CuInEuS<sub>2</sub>) LBNPs. Given that the DLS size of these particles is well below the pore size of the syringe filter, it is unlikely that LBNPs were excluded during filtration. The LBNPs were injected to hu mice at the dosage equivalent to 1000 μCi/kg by the tail vein. The biodistribution of radio-labeled LBNPs was acquired at 6, 24, and 48 h of post-injection using the PET bioimaging system

(MOLECUBE β-CUBE, NV, Ghent, Belgium). The co-registration of 3D computed tomography (CT) and PET was performed by using VivoQuant 3.5 software (Invivo Boston, MA, USA). At 48 h post-injection, mice were sacrificed, and major organs were collected, weighed, and measured the radioactivity using gamma scintillation spectrometry (Hidex Automatic Gamma Counter, Turku, Finland). The radioactivity count percent was determined by following Eq-3.

$$\text{Radioactivity count(\%/g)} = \frac{(\text{organ radioactivity count} \times 100)}{(\text{total radioactivity count} \times \text{organ weight})} \quad (3)$$

To determine the biodistribution of RPV, the nonradioactive LBNPs were injected at the dose of 25 mg/kg equivalent to RPV via the tail vein. At 24 h of post-injection, mice were sacrificed, and liver, spleen, and blood plasma samples were collected for RPV quantification by electrospray ionization mass spectrometry (Waters ACQUITY Premier UPLC, Xevo TQ-XS tandem quadrupole mass spectrometer, MA, USA)

To conduct the brain distribution study, hu mice were anesthetized and prepared for the focused ultrasound (FUS) procedure. This involved removing the scalp hair and inserting a 26-gauge intravenous catheter into the tail vein. After stereotaxic localization of the bregma, 100 μL of Definity® microbubble solution (1:1000 dilution by volume) was immediately injected before the FUS. The FUS with optimized parameters (500 kHz frequency, 1.0 W power, 10% duty cycle, and 75 s duration) was then applied to each mouse hemisphere (+/- 2.5 mm of bregma). After the FUS, LBNPs were immediately infused slowly through the tail vein catheter. The animal was then taken to the 9.4 Tesla MR scanner (Biospec Avance III Bruker MR scanner) for verification of the blood-brain barrier disruption (BBBd) with T1-weighted MRI before and after intravenous gadolinium infusion (25% dilution). On the following day, the IVIS (Xenogen Corporation, Alameda, CA) was performed to assess the brain distribution of LBNPs and compare those with or without FUS. Following perfusion and euthanasia, we performed immunofluorescence evaluations on the brain tissue. This included staining for all nuclei (DAPI), microglia (IBA-1), and human nuclei (HuNu).

### HIV-1 suppression in hu mice

Hu mice with an average age between 18 to 20 weeks were infected with 1.5 × 10<sup>4</sup> TCID<sub>50</sub> of HIV-1<sub>ADA</sub> via intraperitoneal injection. At 2 weeks post-infection, blood samples were collected via sub-mandibular vein bleeding, blood plasma was 10-fold diluted in AcroMetrix™ EDTA plasma dilution matrix (Catalog # S2284, Thermo Scientific, USA) and subjected to viral load determination using automated COBAS Ampliprep V2.0/Taqman-48 system (Roche Molecular Diagnostics, Basel, Switzerland). After confirmation of plasma viral load, mice were separated into three groups: HIV-1 infected and untreated control, LBNP-RPV, and LBNP-RPV-CCR5. LBNPs were injected via tail vein at the dose of 25 mg/kg RPV equivalent. The body weight and plasma viral load were determined on days 0 and 7 and 14 of post-LBNP injection. On day 14 of post-LBNP injection, the mice were terminated, and blood and major organs were collected. Blood samples were used for whole blood cell count (by Abaxis VetScan HM5) and serum chemistry (by Abaxis VetScan VS2), and the tissues from the major organs were fixed, paraffin-embedded, and stained with hematoxylin and eosin (H&E) and HIV-1p24 antibody. The histological images of different tissues were captured on a Nuance EX multispectral imaging system affixed to a Nikon Eclipse E800 microscope.

### Statistical analysis

The statistical analysis was performed using Prism 10 (GraphPad Prism 10.2.2.397, GraphPad Software, Inc., San Diego, CA) on the data from at least three independent experiments, as specified. Data are presented as mean ± standard deviation. The statistical difference between the two groups was analyzed using an unpaired t-test. The *p* < 0.05 was

considered statistically significant. Statistical significance was assessed by an unpaired or one-way ANOVA. \* $P \leq 0.05$ , \*\* $P \leq 0.01$ , \*\*\* $P \leq 0.001$ , and \*\*\*\* $P \leq 0.0001$  were considered significant.

### Reporting summary

Further information on research design is available in the Nature Portfolio Reporting Summary linked to this article.

### Data availability

All data generated or analyzed during this study are included in this article and its Supplementary information files. Materials used in the analysis are available upon request from the corresponding author. The supporting information contains the selected area electron diffraction, energy dispersive X-ray spectroscopic, and X-ray photoelectron spectroscopic results of the nanoprobe. It also includes the NMR and mass spectroscopy of the CCR5 conjugated DSPE-PEG, MVC cell viability, uptake of LBNP-RPV in MDMs, and radiolabeled stability of LBNPs. Source data are provided with this paper.

### References

- Khan, N. H. et al. Assessment of knowledge and attitudes related to hiv/aids among the population with increasing incidence rate. *Cureus* **16**, e53451 (2024).
- Bekker, L.-G. et al. HIV infection. *Nat. Rev. Dis. Prim.* **9**, 42 (2023).
- Holmes, E. C. On the origin and evolution of the human immunodeficiency virus (HIV). *Biol. Rev.* **76**, 239–254 (2001).
- Chun, T.-W., Moir, S. & Fauci, A. S. HIV reservoirs as obstacles and opportunities for an HIV cure. *Nat. Immunol.* **16**, 584–589 (2015).
- Senapathi, J., Bommakanti, A., Mallepalli, S., Mukhopadhyay, S. & Kondapi, A. K. Sulfonate modified Lactoferrin nanoparticles as drug carriers with dual activity against HIV-1. *Colloids Surf. B Biointerfaces* **191**, 110979 (2020).
- Singh, A. et al. Laser ablation for pharmaceutical nanoformulations: Multi-drug nanoencapsulation and theranostics for HIV. *Nanomedicine* **25**, 102172 (2020).
- Fotooh Abadi, L., Kumar, P., Paknikar, K., Gajbhiye, V. & Kulkarni, S. Tenofovir-tethered gold nanoparticles as a novel multifunctional long-acting anti-HIV therapy to overcome deficient drug delivery: an in vivo proof of concept. *J. Nanobiotechnology* **21**, 19 (2023).
- Surve, D. H., Jirwankar, Y. B., Dighe, V. D. & Jindal, A. B. Long-acting efavirenz and hiv-1 fusion inhibitor peptide co-loaded polymer-lipid hybrid nanoparticles: statistical optimization, cellular uptake, and in vivo biodistribution. *Mol. Pharm.* **17**, 3990–4003 (2020).
- Vasukutty, A., et al. CXCR4 targeting nanoplatform for transcriptional activation of latent HIV-1 infected T cells. *ACS Appl. Bio. Mater.* (2023).
- Gunaseelan, S., Gunaseelan, K., Deshmukh, M., Zhang, X. & Sinko, P. J. Surface modifications of nanocarriers for effective intracellular delivery of anti-HIV drugs. *Adv. Drug Deliv. Rev.* **62**, 518–531 (2010).
- Eshaghi, B., Fofana, J., Nodder, S. B., Gummuluru, S. & Reinhard, B. M. Virus-mimicking polymer nanoparticles targeting cd169(+) macrophages as long-acting nanocarriers for combination anti-retrovirals. *ACS Appl Mater. Interfaces* **14**, 2488–2500 (2022).
- Menon, I., Zaroudi, M., Zhang, Y., Aisenbrey, E. & Hui, L. Fabrication of active targeting lipid nanoparticles: Challenges and perspectives. *Mater. Today Adv.* **16**, 100299 (2022).
- Dash, P. K. et al. CRISPR editing of CCR5 and HIV-1 facilitates viral elimination in antiretroviral drug-suppressed virus-infected humanized mice. *Proc. Natl Acad. Sci. USA* **120**, e2217887120 (2023).
- Daraban, L., Cozar, O., Fiat, T. & Daraban, L. The Production and Characterization of some medically used Radioisotopes. *Ann. West Univ. Timis. Phys. Ser.* **48**, 118 (2006).
- Herskovitz, J. et al. Europium sulfide nanoprobe predicts anti-retroviral drug delivery into HIV-1 cell and tissue reservoirs. *Nano-theranostics* **5**, 417 (2021).
- Polianova, M. T., Ruscetti, F. W., Pert, C. B. & Ruff, M. R. Chemokine receptor-5 (CCR5) is a receptor for the HIV entry inhibitor peptide T (DAPTA). *Antivir. Res.* **67**, 83–92 (2005).
- Pang, B. et al. 64Cu-doped PdCu@ Au tripods: a multifunctional nanomaterial for positron emission tomography and image-guided photothermal cancer treatment. *ACS nano* **10**, 3121–3131 (2016).
- Hu, M., Li, X., You, Z., Cai, R. & Chen, C. Physiological barriers and strategies of lipid-based nanoparticles for nucleic acid drug delivery. *Adv. Mater.* **36**, 2303266 (2024).
- Zalba, S., Ten Hagen, T. L., Burgui, C. & Garrido, M. J. Stealth nanoparticles in oncology: Facing the PEG dilemma. *J. Controlled Release* **351**, 22–36 (2022).
- Kruize, Z. & Kootstra, N. A. The role of macrophages in HIV-1 persistence and pathogenesis. *Front. Microbiol.* **10**, 484054 (2019).
- Wong, M. E., Jaworowski, A. & Hearn, A. C. The HIV reservoir in monocytes and macrophages. *Front. Immunol.* **10**, 456992 (2019).
- Meng, F.-Z. et al. TLR7 activation of macrophages by imiquimod inhibits HIV infection through modulation of viral entry cellular factors. *Biology* **10**, 661 (2021).
- Veenhuis, R. T. et al. Monocyte-derived macrophages contain persistent latent HIV reservoirs. *Nat. Microbiol.* **8**, 833–844 (2023).
- Brož, P. et al. Cell targeting by a generic receptor-targeted polymer nanocontainer platform. *J. controlled release* **102**, 475–488 (2005).
- Denton, P. W. & García, J. V. Humanized mouse models of HIV infection. *AIDS Rev.* **13**, 135–148 (2011).
- Kevadiya, B. D. et al. Rod-shape theranostic nanoparticles facilitate antiretroviral drug biodistribution and activity in human immunodeficiency virus susceptible cells and tissues. *Theranostics* **10**, 630–656 (2020).
- Dilliard, S. A. & Siegwart, D. J. Passive, active and endogenous organ-targeted lipid and polymer nanoparticles for delivery of genetic drugs. *Nat. Rev. Mater.* **8**, 282–300 (2023).
- Wang, X., Russell-Lodrigue, K. E., Ratterree, M. S., Veazey, R. S. & Xu, H. Chemokine receptor CCR5 correlates with functional CD8(+) T cells in SIV-infected macaques and the potential effects of maraviroc on T-cell activation. *Faseb j.* **33**, 8905–8912 (2019).
- Ren, J. et al. Chemical and biophysical signatures of the protein corona in nanomedicine. *J. Am. Chem. Soc.* **144**, 9184–9205 (2022).
- Dilliard, S. A. et al. The interplay of quaternary ammonium lipid structure and protein corona on lung-specific mRNA delivery by selective organ targeting (SORT) nanoparticles. *J. Controlled Release* **361**, 361–372 (2023).
- Mandal, S. et al. Targeted immuno-antiretroviral to promote dual protection against HIV: a proof-of-concept study. *Nanomaterials* **12**, 1942 (2022).
- Burgess, A., Shah, K., Hough, O. & Hynynen, K. Focused ultrasound-mediated drug delivery through the blood-brain barrier. *Expert Rev. Neurother.* **15**, 477–491 (2015).
- Necula, D., Riviere-Cazaux, C., Shen, Y. & Zhou, M. Insight into the roles of CCR5 in learning and memory in normal and disordered states. *Brain Behav. Immun.* **92**, 1–9 (2021).
- Herskovitz, J. et al. CRISPR-Cas9 mediated exonic disruption for HIV-1 elimination. *EBioMedicine* **73**, 103678 (2021).
- Panja, S. <https://BioRender.com/o53x373> [biorender.com] (2024).

### Acknowledgements

The University of Nebraska Foundation supported the work, including donations from Carol Swarts, M.D. Emerging Neuroscience Research Laboratory, and the Margaret R. Larson Professorship. The research received support from National Institutes of Health grants 5R01MH121402, 1R01A1158160, R01 DA054535, PO1 DA028555, R01 NS126089, R01 NS36126, PO1 MH64570, P30 MH062261, 2R01 NS034239 and DP1-DA53719, Lantheus for providing the Definity microbubbles (CG#22002), and UNMC student assistantship/fellowship. The authors are thankful to Dr. Benson Edagwa for his thoughtful

comments and suggestions and Emiko Waight for the development and technical assistance provided for this work. The authors thank Guo Lili and Edward Makarov for their kind help in generating the humanized mice. The authors are also thankful to Drs. Brady Sillman, and Nayan Mohammad Ullah for their assistance in analyzing the RPV levels in plasma and tissues. The authors thank Mrs. Tom Barger and Nicholas Conoan for their technical assistance in performing the TEM. The authors are also thankful to Drs. Bala Balasubramanian, Shah Valloppilly, and Lanping Yue thank you for your help performing the XPS and XRD. Ben Atkinson, Segun Bernard, Dr. Prathibha Meesala, and Eric Cunningham provided bioimaging and histological support and were responsible for maintaining the humanized mouse colonies.

### Author contributions

S.P. and M.P. designed and performed the experiments. L.A.Z., P.Y., and S.B. assisted in performing the experiments. L.C., P.W., and A.H. performed FUS and brain histologies. S.P. and H.E.G. provided experimental oversight, data interpretation, and guidance. S.C. evaluated the histopathology. B.D.K. assisted in the design and formulation of the radioactive nanoprobe. S.G. assisted in the generation of humanized mice. B.H. performed drug tissue level analysis. S.P., H.E.G., and M.P. wrote and edited the manuscripts. All authors have read and approved the final version of the manuscript.

### Competing interests

The authors declare that Dr. Howard Gendelman co-founder of Exavir Therapeutics, Inc. The biotechnology company is developing ultra-long-acting drugs. The drugs in development are not linked to those created in the current report. All other authors declare no competing interests.

### Additional information

**Supplementary information** The online version contains supplementary material available at <https://doi.org/10.1038/s41467-024-55544-9>.

**Correspondence** and requests for materials should be addressed to Sudipta Panja or Howard E. Gendelman.

**Peer review information** *Nature Communications* thanks Eden Tanner, who co-reviewed with Duoyi Hu, Yujia He and the other, anonymous, reviewer(s) for their contribution to the peer review of this work.

**Reprints and permissions information** is available at <http://www.nature.com/reprints>

**Publisher's note** Springer Nature remains neutral with regard to jurisdictional claims in published maps and institutional affiliations.

**Open Access** This article is licensed under a Creative Commons Attribution-NonCommercial-NoDerivatives 4.0 International License, which permits any non-commercial use, sharing, distribution and reproduction in any medium or format, as long as you give appropriate credit to the original author(s) and the source, provide a link to the Creative Commons licence, and indicate if you modified the licensed material. You do not have permission under this licence to share adapted material derived from this article or parts of it. The images or other third party material in this article are included in the article's Creative Commons licence, unless indicated otherwise in a credit line to the material. If material is not included in the article's Creative Commons licence and your intended use is not permitted by statutory regulation or exceeds the permitted use, you will need to obtain permission directly from the copyright holder. To view a copy of this licence, visit <http://creativecommons.org/licenses/by-nc-nd/4.0/>.

© The Author(s) 2025